Design, Development, and Clinical Validation of a Two Degrees of Freedom Compliant Ankle-Foot Prosthesis Based on a 4-4R Parallel Mechanism

Haohua Xiu[a], Yang Han[b], Xu Wang[a], Yao Zhang[a], Wei Liang[a],

Guowu Wei[c], Lei Ren[a,d], Luquan Ren[a]

[a] Key Laboratory of Bionic Engineering, Ministry of Education, Jilin University, Changchun 130025 China.

[b] School of Mechanical and Aerospace Engineering, Jilin University, Changchun 130025, China.

[c] School of Computing, Science and Engineering, University of Salford, Salford M5 4WT, UK.

[d] School of Mechanical, Aerospace and Civil Engineering, The University of Manchester, Manchester M13 9PL, UK

Corresponding authors: Lei Ren and Guowu Wei

E-mail addresses: xiuhh@jlu.edu.cn (H. Xiu), hanyang19@mails.jlu.edu.cn (Y. Han), wx19@mails.jlu.edu.cn (X. Wang), yaoz20@mails.jlu.edu.cn (Y. Zhang), weiliang@jlu.edu.cn (W. Liang), g.wei@salford.ac.uk (G. Wei), lei.ren@manchester.ac.uk (L. Ren), lqren@jlu.edu.cn (LQ. Ren)

Abstract

Compared with active prostheses, passive compliant ankle prostheses offer the advantages of reduced energy consumption, a lighter weight, a simple structure, and lower costs. However, although various commercial products are available, these designs do not provide adequate degrees of freedom (DOFs) for movement. This paper presents a compliant passive ankle–foot prosthesis (CPAF) capable of 2-DOF rotation during locomotion. The CPAF uses a 2-DOF parallel mechanism to support the bodyweight and offer limited rotation during movement, and it incorporates a compliant component to facilitate and generate torque to conform to uneven terrains. The kinematics of the parallel mechanism, including the workspace and singularities, were investigated. A prototype was developed, and a performance evaluation showed that sufficient torque was generated with an appropriate range of motion. A clinical validation was conducted: the dynamic analysis indicated that the CPAF provided good gait movement and generated sufficient ankle torque during level-ground walking, and the metabolic test demonstrated the configuration 4 of the compliant component performs the most efficiency during walking.

1 Introduction

The ankle joint plays a critical role in daily life. Below-knee amputees suffer from reduced ankle push-off and are left with the substantial challenge of adapting self-

control strategies to compensate for the functional loss of the plantar flexors [1]. This compensation increases the locomotion cost and stresses on the knee, hip, and contralateral ankle joints, which causes long-term health issues and comorbidities due to the asymmetrical joint loading [2]. The most commonly used ankle–foot prosthesis is the solid ankle cushioned heel (SACH), which closely resembles the shape of an actual foot and focuses primarily on reducing the impact load during movement. However, it stores and releases very little elastic energy at push-off and it does not provide enough range of motion. The dynamic response ankle foot or energy storage and return (ESR) foot [3] is based on a stiff carbon fiber board. Like an Achilles tendon, it provides passive flexion for storing energy during the beginning of gait cycle and returns the energy to propel the foot forward during push-off to help transition the center of mass over the leading limb. However, making an ESR foot as flexible as an intact foot is still a delicate challenge. Increasing the stiffness increases the propulsion force but also decreases the range of motion of the ankle, which helps accommodate sloped surfaces [4], maintain a lower center of gravity, increase the step length of the intact limb [3, 5] and step time of individuals recovering from sprained ankles, and improve stance mechanics [6].

Many ankle–foot prostheses have only been designed to exhibit the range of motion experienced by the intact ankle during walking on an even surface, which is generally less than 30° [7]. A novel passive ankle–foot prosthesis was developed that can mimic the angles and ground reaction forces of an able-bodied ankle [5]. A hydraulic ankle was proposed that facilitates a greater range of motion than a rigid ankle device by compensating for the total mechanical work and kinematic [8]. Compared to passive ankle–foot prostheses, active prostheses use microprocessors to obtain the desired kinematics and kinetics. However, current active prostheses struggle to provide the necessary power while matching the size and weight of an able-bodied ankle and foot [9]. In addition, the able-bodied ankle and foot have no net external energy losses at normal walking speeds over level ground. Hence, a passive prosthesis is potentially sufficient for daily movement [10]. Increasing the degrees of freedom (DOFs) can help an ankle–foot prostheses better mimic a natural ankle joint and provide comfortable walking, especially on undulating and rough terrains. Hence, 2-DOF mechanisms (i.e., inversion and eversion) are being designed to provide ankle–foot prostheses with a sufficient range of motion. Such 2-DOF mechanisms have been extensively studied and applied in various fields, such as beam steering devices [11, 12], aerospace antennas [13, 14], stabilized platforms [15], and robotic joints [16-21].

Conventionally, 2-DOF mechanisms are adopted and used as pointing systems, the simplest one is the serial gimbal structure with inner and outer gimbal axes. Although these platforms have simple mechanical models, they have a small payload and suffer from gimbal lock [22, 23]. In addition, gimbal structures have little internal space for deploying an elastic component to facilitate compliant mechanisms. This has led researchers to consider parallel mechanisms owing to their advantages of high precision, high stiffness, and high loading capacity [24, 25]. In contrast to serial gimbal mechanisms, spherical parallel mechanisms exhibit favorable features for pointing applications because they can distribute the load exerted on the moving platform to the

kinematic chains [22].

To achieve a larger operational (pointing and tracking) range, Ross-Hime Designs® [26] developed a 2-DOF parallel mechanism called the Omni-Wrist III, which is a robotic manipulator inspired by the kinematics of the human wrist. Omni-Wrist III is characterized by the actuators not being located in the joints but rather attached to the links, which mimics the attachment of muscles to bones in biological structures. This design eliminates the gears conventionally needed to convert translational motion into rotational motion, so the moving platform of this device is not impaired by backlash [27, 28]. Sofka [27, 29] used the conventional Denavit–Hartenberg method to investigate the direct kinematics of Omni-Wrist III and developed a control system for application to the laser beam steering devices. Yu [30] discussed the mobility and singularity of Omni-Wrist III based on reciprocal screw system theory and explored the axode characteristics [31] to extend the design to new spherical gears and constant-velocity couplings.

To the best knowledge of the authors, the parallel mechanisms with two degrees of freedom of rotation have only been practically used for pointing applications like laser beam steering devices, manipulation simulator and structural frame of robotic wrist. There has no report nor published research about using such kind of mechanism in lower limb prosthetic devices yet. In this study, we applied and combined the typical 2-DOF parallel mechanism (Omni-Wrist III) with a compliant component and an ESR foot to realize a compliant passive ankle–foot prosthesis (CPAF) that can assist patients with achieving a natural gait motion. The Omni-Wrist III structure has been detailed designed and assembled, so that the range of motion can be determined by the kinematics analysis and the characteristics of the ankle motion during walking. The proposed design facilitates and generates torques in dorsiflexion, plantarflexion, inversion, and eversion to conform with uneven terrain.

The rest of this paper is organized as follows. Section 2 describes the structure of Omni-Wrist III and presents a kinematic analysis on its geometry, including the workspace and singularities. Section 3 presents the design and prototype of the proposed CPAF, which includes the assembly of the Omni-Wrist III mechanism and the design/fabrication of the compliant components. Section 4 presents the performance evaluation of the proposed CAPF in accordance with the GB 14723-2008 standard. Section 5 presents a clinical study and evaluation of the proposed CAPF with a focus on the dynamics and metabolic energy consumption of a subject when walking on level ground. Section 6 concludes the paper and discusses future work.

2 Omni-Wrist III: A 4-4R Parallel Mechanism with Equal-Diameter Spherical Motion

The 2-DOF parallel mechanism (PM) has a greatly enhanced pointing capability and range of motion compared with traditional platforms while still satisfying requirements such as a heavy load capacity, high acceleration, and large workspace. Omni-Wrist III is a novel 4–4R (four kinematic chains with four revolute joints in each chain) PM that is capable of executing an equal-diameter spherical pure rotation with a

compact structure. Here, we use the geometric condition method to describe its inverse kinematics with the associated workspace and singularity analyses.

2.1 Structure of the Omni-Wrist III Mechanism

Figure 1(a) shows the detailed geometry of the Omni-Wrist III design, which consists of a fixed base, a moving platform, and four identical kinematic chains. Each kinematic chain connects the fixed base to the moving platform by four revolute joints. Each kinematic chain has three links: two identical L-shaped links and a V-shaped link. Each link has revolute joints at both ends. The V-shaped link is centrally connected to the L-shaped links.

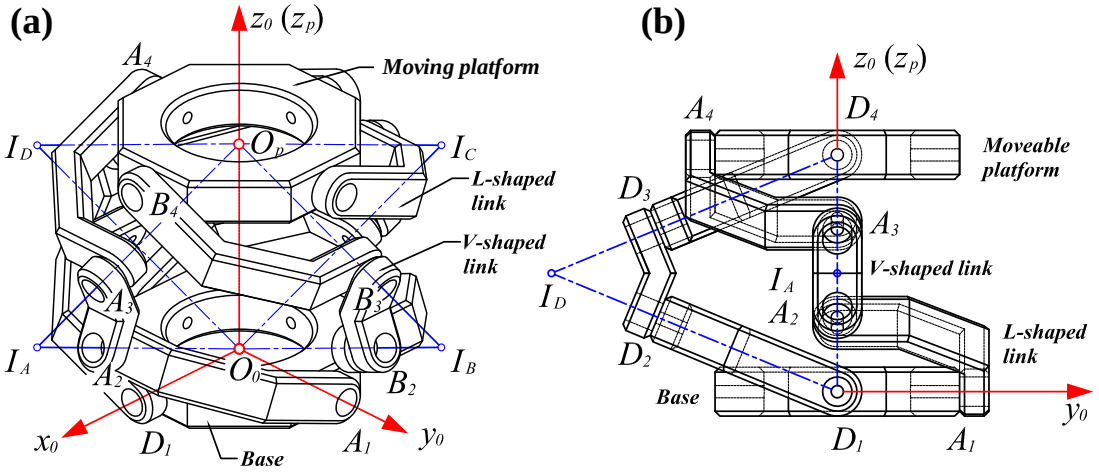

Figure 1 (a) Detailed geometry of Omni-Wrist III and (b) the front view of the mechanism displaying only chain A and chain D.

Kinematic chain A has joints A_1, A_2, A_3, and A_4, which are numbered sequentially from the base to the platform. Similarly, joints B_i, C_i, and D_i (i = 1, 2, 3, 4) form kinematic chains B, C, and D, respectively. To present a clearer visualization of the geometry, Figure 1(b) only shows the two adjacent kinematic chains A and D.

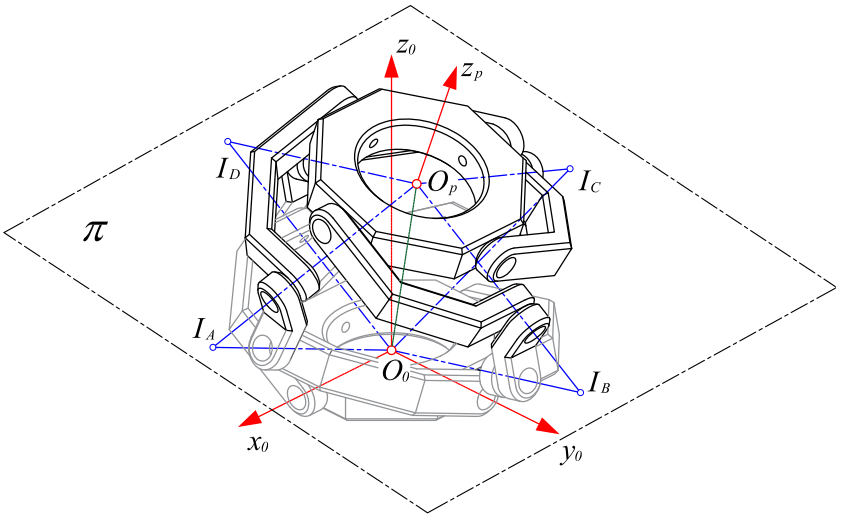

Figure 2 Homo-kinetic symmetry plane π for the configuration of the moving platform rotating about the x_0-axis with respect to the fixed base.

For the V-shaped links in chains A, B, C, and D (denoted as links A_2A_3, B_2B_3, C_2C_3, and D_2D_3), the axes of two joints intersect at point I_k ($k = A$, B, C, and D). Joints A_1, B_1, C_1, and D_1 are adjacently arranged at 90° intervals on the base, and joints A_4, B_4, C_4, D_4 are similarly arranged on the platform. Because the L-shaped links for each kinematic chain are identical, this PM results in a particular configuration where the symmetry plane π is defined by point I_k ($k = 1, 2, 3, 4$). In addition, plane π is always perpendicular to the line formed by the centroids of the base and moving platform (i.e., O_0O_p). The length of line O_0O_p remains unchanged regardless of the configuration; as shown in Figure 2, the moving platform rotates about the x_0-axis with respect to the fixed base.

2.2 Kinematics and Workspace Analysis of the Omni-Wrist III Mechanism

We employed a geometric approach to analyze the kinematics of the moving platform. To derive the position of the moving platform, we established a global coordinate frame $\{O_0–x_0, y_0, z_0\}$ on the fixed base. The origin is at the intersection of the axes of revolute joints A_1 and D_1, the y_0-axis is collinear with the axis of joint A_1, and the x_0-axis lies on the axis of joint D_1 (see Figure 1(a)). Hence, the position of the moving platform can be represented by the coordinates of point O_p, which is determined by any two adjacent revolute joints A_1 and B_1 as inputs. The kinematic model is shown in Figure 3(a).

Let θ_1 and θ_2 be the angles of the inputs (i.e., revolute joints A_1 and B_1). The magnitudes of $\boldsymbol{O_0O_p}$ and $\boldsymbol{O_0I_k}$ ($k = A$, B) are denoted as r and l, respectively. Hence, the coordinates of points I_A and I_B can be written as $I_A = (l\cos\theta_1, 0, l\sin\theta_1)^{\mathrm{T}}$ and $I_B = (0, l\cos\theta_2, l\sin\theta_2)^{\mathrm{T}}$, respectively. The structural parameter γ is defined as the intersection angle of the two axes of the V-shaped link. The orientation of the platform is represented by the angle between the x_0-axis and the projection of line MO_p onto the plane x_0–y_0 (azimuth angle α) and the angle between MO_p and the z_0-axis (pitch angle φ). Hence, the coordinates of O_{p} $(p_{\mathrm{x}}, p_{\mathrm{y}}, p_{\mathrm{z}})^{\mathrm{T}}$ are expressed by the orientation of the platform in the global system:

$$\begin{pmatrix} p_x \\ p_y \\ p_z \end{pmatrix} = \begin{pmatrix} r\sin(\varphi/2)\cos\alpha \\ r\sin(\varphi/2)\sin\alpha \\ r\cos(\varphi/2) \end{pmatrix} = \begin{pmatrix} 2l\sin(\gamma/2)\sin(\varphi/2)\cos\alpha \\ 2l\sin(\gamma/2)\sin(\varphi/2)\sin\alpha \\ 2l\sin(\gamma/2)\cos(\varphi/2) \end{pmatrix} \tag{1}$$

where $r = 2l\sin(\gamma/2)$ can be derived from the isosceles triangle $\triangle O_0I_kO_p$.

Consequently, the pose of the moving platform can be obtained from equation (1):

$$\begin{cases} \alpha = 2\arctan\left(\sqrt{p_x^{\,2} + p_y^{\,2}}\,\Big/\,p_z\right) \\ \varphi = \arctan 2\left(p_y, p_x\right) \end{cases} \tag{2}$$

where $0 < \alpha < 2\pi$ and $0 < \varphi < \pi/2$.

The inverse kinematics is deduced as follows. Owing to the symmetry feature, vector $\boldsymbol{O_0O_p}$ is normal to the symmetry plane π and intersects at midpoint N of O_0O_p. This results in the following constraint equation:

$$\boldsymbol{O_0O_p} \cdot \boldsymbol{I_kN} = 0 \quad (k = A, B) \tag{3}$$

where $\boldsymbol{I}_A\boldsymbol{N} = (p_x/2 - l\cos\theta_1, p_y/2, p_z/2 - l\sin\theta_1)^{\mathrm{T}}$ and $\boldsymbol{I}_B\boldsymbol{N} = (p_x, p_y/2 - l\sin\theta_2, p_z/2 - l\sin\theta_2)^{\mathrm{T}}$.

Equations (1) and (3) can be combined to calculate inputs θ_1 and θ_2:

$$\begin{cases} \theta_1 = \arcsin\left(\dfrac{\sin(\varphi/2)\cos(\varphi/2) - \sin(\varphi/2)\cos\alpha\sqrt{\sin^2(\varphi/2)\cos^2\alpha - \sin^2(\gamma/2) + \cos^2(\varphi/2)}}{\sin^2(\gamma/2) + \sin^2(\varphi/2)\cos^2\alpha} \right) \\ \theta_2 = \arcsin\left(\dfrac{\sin(\varphi/2)\cos(\varphi/2) - \sin(\varphi/2)\sin\alpha\sqrt{\sin^2(\varphi/2)\sin^2\alpha - \sin^2(\gamma/2) + \cos^2(\varphi/2)}}{\sin^2(\gamma/2) + \sin^2(\varphi/2)\sin^2\alpha} \right) \end{cases} \tag{4}$$

Equation (1) can be substituted into equation (4) for calculating the solutions in the set of real numbers:

$$\begin{cases} \sin^2(\varphi/2)\cos^2\alpha \le \sin^2(\gamma/2) \\ \sin^2(\varphi/2)\sin^2\alpha \le \sin^2(\gamma/2) \end{cases} \tag{5}$$

When points I_k of each kinematic chain coincide, mechanism interference occurs. Because we know point I_k is located at the plane generated by moving O_0I_k around axes x_0 and y_0, inputs θ_1 and θ_2 are constrained as follows:

$$\theta_i \in \left(-\frac{1}{2}\pi, \frac{1}{2}\pi \right) \quad i = 1, 2 \tag{6}$$

By substituting equation (4) into equation (6), we obtain the interference constraint conditions for the links:

$$\begin{cases} -1 < \dfrac{\sin(\varphi/2)\cos(\varphi/2) - \sin(\varphi/2)\cos\alpha\sqrt{\sin^2(\varphi/2)\cos^2\alpha - \sin^2(\gamma/2) + \cos^2(\varphi/2)}}{\sin^2(\gamma/2) + \sin^2(\varphi/2)\cos^2\alpha} < 1 \\ -1 < \dfrac{\sin(\varphi/2)\cos(\varphi/2) - \sin(\varphi/2)\sin\alpha\sqrt{\sin^2(\varphi/2)\sin^2\alpha - \sin^2(\gamma/2) + \cos^2(\varphi/2)}}{\sin^2(\gamma/2) + \sin^2(\varphi/2)\sin^2\alpha} < 1 \end{cases} \tag{7}$$

once the input angles are constrained by $\theta_i < \pi/2$ (i = 1, 2), the workspace can be determined by using equation (5), which can be rewritten as follows:

$$\begin{cases} \gamma < 2\arccos\left|-\sin(\varphi/2)\sin\alpha\right| & \textit{for chain } 1 \\ \gamma < 2\arccos\left|\sin(\varphi/2)\cos\alpha\right| & \textit{for chain } 2 \end{cases} \tag{8}$$

We conclude that $\varphi + \gamma > \pi$ and $\varphi_{\max} = \pi - \gamma$ where $0 < \alpha < 2\pi$. When l = 48 mm and γ = 45°, the topological workspace (scenario 1) can be programmed in MATLAB®, as shown in Figure 3(b). When the thickness of the linkages and height of the bolt head for connecting linkages are considered (scenario 2), inputs θ_1 and θ_2 are both constrained in the range of [13.7°, 31°]. This reduces the workspace, as shown in Figure 3(c), and the range of φ is limited to [0, 25.11°].

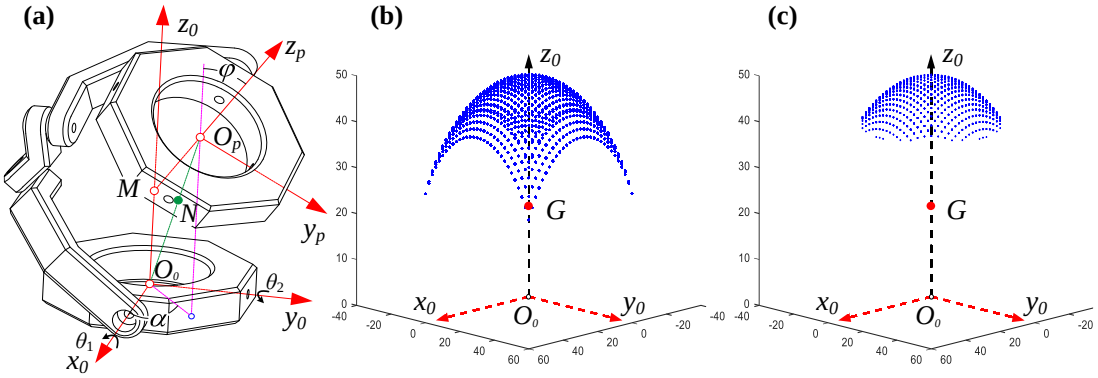

Figure 3 (a)The orentation representation of the moving platform in an arbitrary configuration. (b) Workspace in scenario 1: topological workspace at $l = 48$ mm and $\gamma = 45°$. (c) Workspace in scenario 2: interference due to the thickness of the linkage and height of the bolt head.

Owing to the 2-DOF characteristics, the moving platform has two motion patterns [31] to reach any position in scenario 2 with the specified orientation, as shown in Figure 4(a) and (b). In the first pattern, the fixed base has a fixed axode. The moving platform generates a moving axode by rolling clockwise or counterclockwise around point M. The fixed and moving axodes are conical surfaces. In the second pattern, the moving platform rolls about a specified axis, and both axodes are cylindrical surfaces. The moving axode in the two patterns rolls on the fixed axode and intersects line O_0O_p at point N without sliding. This means that the moving platform cannot rotate about line O_0O_p at any instant. This is called an equal-diameter rolling motion [32-34].

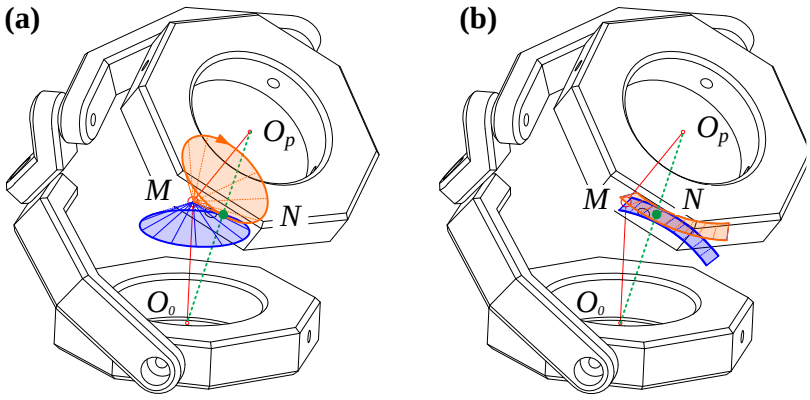

Figure 4 In scenario 2: (a) clockwise rolling movement around point M with associate conical axodes and (b) rolling movement of the moving platform about a specified axis that forms the cylindrical axodes.

2.3 Singularity Analysis

A vector method [35] was used for singularity analysis. Generalizing the geometric constraint equation (3) and taking the derivative with respect to time obtains

$$\begin{cases} f\left(\boldsymbol{\theta}, \mathbf{P}\right) = 0 \\ \mathbf{J}_\theta \dot{\boldsymbol{\theta}} = \mathbf{J}_p \dot{\mathbf{P}} \end{cases} \tag{9}$$

where $\dot{\boldsymbol{\theta}} = (\dot{\theta}_1, \dot{\theta}_2)^{\mathrm{T}}$ is the velocities of input revolute joints A_1 and B_1 and, $\dot{\mathbf{P}} = (\dot{\alpha}, \dot{\varphi})^{\mathrm{T}}$

is the orientation velocities of the moving platform. A serial-singularity configuration occurs when $\det(\mathbf{J}_\theta) = 0$, which implies that such singularities are obtained at the boundary of the moving platform's workspace. This results in

$$\mathbf{J}_\theta = \begin{pmatrix} \dfrac{\partial f_1}{\partial \theta_1} & 0 \\ 0 & \dfrac{\partial f_2}{\partial \theta_2} \end{pmatrix} \tag{10}$$

where $\partial f_1/\partial\theta_1=\sin(\varphi/2)\cos\alpha\sin\theta_1-\cos(\varphi/2)\cos\theta_1$ and $\partial f_2/\partial\theta_2=\sin(\varphi/2)\sin\alpha\sin\theta_2-\cos(\varphi/2)\cos\theta_2$. If we simplify the above equations, then we can conclude that neither $\partial f_1/\partial\theta_1$ nor $\partial f_1/\partial\theta_2$ equals zero. Hence, this mechanism does not have a serial-singularity configuration.

Parallel singularity occurs when the position of the moving platform is no longer controllable; the moving platform can rotate freely if the actuated joints A_1 and B_1 are locked. This situation results in

$$\mathbf{J}_\theta = -\begin{pmatrix} \dfrac{\partial f_1}{\partial \alpha} & \dfrac{\partial f_1}{\partial \varphi} \\ \dfrac{\partial f_2}{\partial \alpha} & \dfrac{\partial f_2}{\partial \varphi} \end{pmatrix} \tag{11}$$

where

$$\begin{cases} \dfrac{\partial f_1}{\partial \alpha} = \sin(\varphi/2)\sin\alpha\cos\theta_1 \\ \dfrac{\partial f_1}{\partial \varphi} = -\dfrac{1}{2}\cos(\varphi/2)\cos\alpha\cos\theta_1 + \dfrac{1}{2}\sin(\varphi/2)\sin\theta_1 \\ \dfrac{\partial f_2}{\partial \alpha} = -\sin(\varphi/2)\cos\alpha\cos\theta_2 \\ \dfrac{\partial f_2}{\partial \varphi} = -\dfrac{1}{2}\cos(\varphi/2)\sin\alpha\cos\theta_2 + \dfrac{1}{2}\sin(\varphi/2)\sin\theta_2 \end{cases} \tag{12}$$

When $\varphi = 0$, $\partial f_1/\partial\alpha = \partial f_2/\partial\alpha = 0$, and $\det(\mathbf{J}_\theta) = 0$, the mobility of the moving platform does not change. When $\theta_1 = \theta_2 = 0$, the pitch angle φ becomes 45°, which leads to $\det(\mathbf{J}_\theta) = 0$. Under this circumstance, if there are only two input kinematic chains, then the axes of joints A_3 and B_4 are co-linear, and the axes of joints A_4 and B_3 are also co-linear. If a third kinematic chain exists (e.g., chain $C_1C_2C_3C_4$) for which the axis of the first revolute joint C_1 is perpendicular to any axis of the input joint A_1 or B_1, this gives the moving platform an extra instantaneous rotation about the common axis of joints A_3, B_4, and C_4. However, Omni-Wrist III has a redundant fourth kinematic chain that constrains the instantaneous rotation. Therefore, this mechanism does not have a parallel-singularity configuration.

3 Design and Prototype of the Proposed 2-DOF Compliant Passive Ankle-Foot Prosthesis

The above kinematic analysis shows that Omni-Wrist III can be applied as a lower-limb prosthetic joint. It is characterized by a 2-DOF moving platform with an unchanging radius when the platform rotates along two planes perpendicular to each other. In other words, the base of Omni-Wrist III can be fixed to a pylon, and the foot keel can be mounted to the moving platform. By taking appropriate design in linkage parameter, one of the benefits is that the center of rotation of Omni-Wrist III is similar to the human body. To implement ankle motion and energy return, we designed and fabricated a series of elastomer support blocks and placed them inside the Omni-Wrist III structure. The Omni-wrist III structure supports the body weight during the stance phase, and the elastomer support block contributes damp natural gait. With the help of carbon fiber foot keel, the proposed ankle prosthesis can assist amputees in achieving natural gait motion which includes: dorsiflexion, plantarflexion, inversion, eversion and impact absorption. Figure 5 shows a schematic of the proposed 2-DOF compliant passive ankle-foot prosthesis (referred to simply as "2-DOF CPAF" with ESR foot and "2-DOF CPA" without ESR foot). The geometric and structural parameters of the designed 2-DOF parallel mechanism (Omni-Wrist III) used in the CPAF prototype including the parameters of the overall structure and each link are illustrated and listed in Appendix A.

The 2-DOF CPAF comprises three parts. The Omni-Wrist III mechanism provides support and constrains the position. The polyurethane rubber block facilitates and generates torques in dorsiflexion, plantarflexion, inversion, and eversion to conform to uneven terrain. The carbon fiber foot keel (Tehlin™) provides shock absorption, foot flexion, and strain energy storage and release during walking. We utilized four grub screws to fix the moving platform and fixed base to the top and bottom, respectively, of the polyurethane rubber block. For the rotation, we used a shoulder screw with two nylon spacers to connect the V-shaped link to the L-shaped links and the L-shaped links to the moving platform or fixed base. One oil-free bushing was employed to provide adequate lubrication.

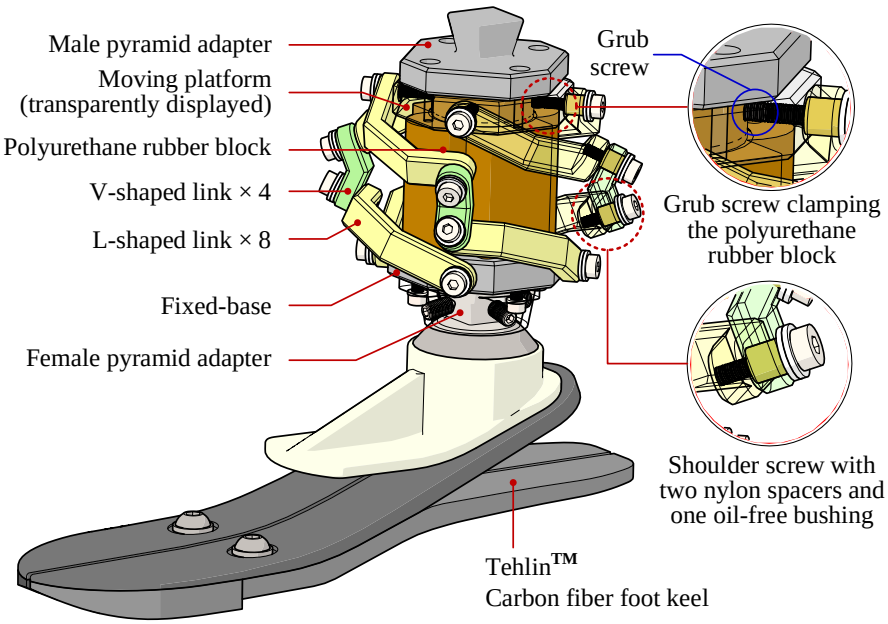

Figure 5 Schematic of the proposed 2-DOF CPAF. The net weight is 1.05 kg. The height from the

top of the male adapter to the bottom of the female adapter is 157 mm, and the height from the top of the male adapter to the foot keel is 93 mm. The width is 76.5 mm.

A typical gait cycle for a foot comprises two phases: stance and swing. A proper ankle prosthesis with a foot keel should be able to store energy to mimic the motion of an intact foot. We designed the passive 2-DOF CPAF by mainly focusing on the stance phase. When the 2-DOF CPAF hits the ground, the flexibility of the carbon fiber keel allows it to absorb the shock induced by the terrain. The 2-DOF CPAF and its keel continue to deflect and store the maximum elastic energy when the amputee stands with the prosthesis flat on the ground. Dorsiflexion during the stance phase releases part of the energy in the heel, which is partly transferred to the keel. The 2-DOF CPAF and keel accumulate mechanical energy in elastic structures in the early- to mid-stance phases; the energy is then transferred back to the amputee to propel the body forward in the late-stance phase (i.e., toe-off). Hence, we designed the support block inside Omni-Wrist III according to the following principles:

(1) The elastomer support block requires sufficient hardness and resilience to avoid triggering unintentional actions during walking that can lead to instability.

(2) The range of eversion should be limited without affecting dorsiflexion and plantarflexion.

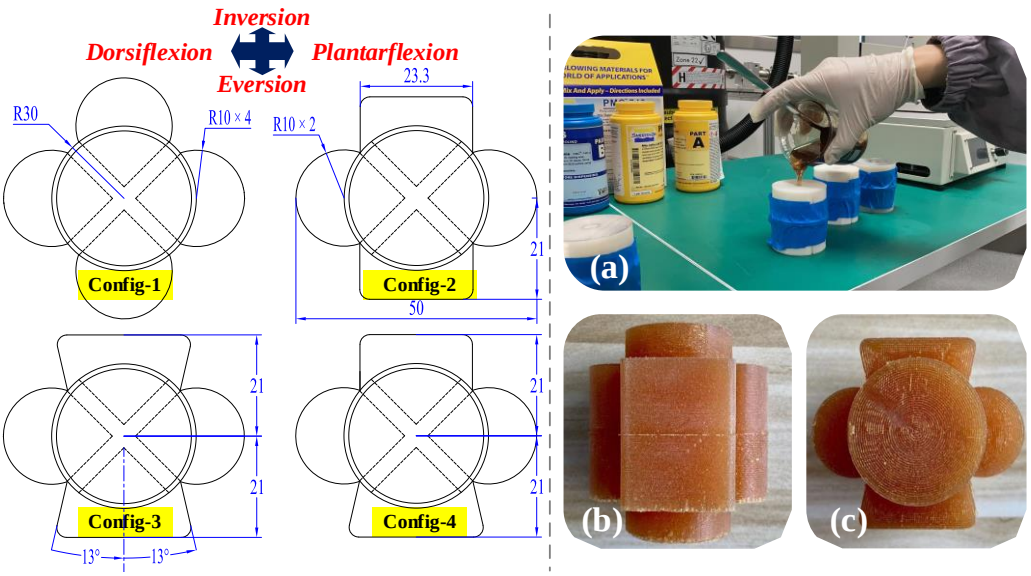

Figure 6 Design and fabrication of polyurethane rubber blocks. Left: four cross-sectional shapes with different parameters for the support blocks (configurations 1–4, unit: mm). Right: (a) liquid polyurethane poured in a mold. (b) Front view and (c) top view of one of the fabricated polyurethane rubber blocks (configuration 3).

To comply with design principle 1, we fabricated support blocks from Smooth-On™ polyurethane rubber compound PMC™ 790, which offers superior tear and tensile strength, impact, and abrasion resistance with sufficient hardness (90A) and resilience after bending. The support blocks were designed to have a column-like structure with a protuberant structure around the craniocaudal axis in the transverse plane. The upper surface of the protuberant structure was in contact with the lower surface of the moving platform. Similarly, the lower surface of the protuberant structure was in contact with

the upper surface of the fixed base. To comply with design principle 2, we designed four different cross-sectional shapes for the protuberant structure labeled as configurations 1–4 (see the left part of Figure 6). The four configurations generated different torques that affected the amplitude of specific ankle motions. Each configuration had an identical shape (approximately circular) for dorsiflexion and plantarflexion. In configuration 1, the shapes for inversion and eversion were similar to the shapes for dorsiflexion and plantarflexion. In configuration 2, the shapes for inversion and eversion changed to rectangles. In configuration 3, the shapes for inversion and eversion changed to trapezoids. In configuration 4, the shape for inversion was a rectangle, and the shape for eversion was a trapezoid. Design principle 2 was achieved by ensuring that the cross-sectional area of four configurations during eversion was no less than the area during other bendings. The support blocks were fabricated as follows:

Step 1: Measuring and mixing

Liquid polyurethanes are moisture-sensitive and absorb atmospheric moisture. We used a clean beaker as the mixing container and thoroughly mixed Part A and Part B at a 2:1 ratio for at least 3 min.

Step 2: Pouring mold

After 3D printing four molds, we applied the release agent (Universal™ Mold Release) to all surfaces that would contact the rubber to facilitate demolding. A uniform flow (see Figure 6(a)) was used to minimize entrapped air bubbles. We used vacuum degassing to further reduce the amount of entrapped air.

Step 3: Curing

We allowed the polyurethane rubber to cure for at least 48 h at room temperature (23 °C) and replenished the molds to compensate for liquid rubber penetrating the pores of the molds.

Step 4: Post-curing and demolding

After curing, the molds were placed in a plastic bag and put in a thermostatic water tank, which was heated to 65 °C for 4 h to improve the physical properties and performance before demolding.

4 Performance Evaluation

GB 14723-2008 [36] is the experimental standard for evaluating the wearing comfort of ankle–foot prostheses, which is done indirectly by measuring the elastic deformation against the design applying force. First, the male pyramid adapter of the 2-DOF CPAF in configurations 1–4 was clamped to the adjustable angle mounting plate as shown in Figure 7 and Figure 8. It was then vertically loaded by a platen attached to a 400-N load cell (uniaxial tensile test machine, WDGAGE™ WDW-500, China). The angle against the ground was 30° for forefoot bending (Figure 7(a)–(c)) and 15° for heel bending (Figure 7(d)–(f)). The angle against the ground was 0° for both inversion bending (Figure 8(a)–(c)) and eversion bending (Figure 8 (d)–(f)). The punch speed was 50 mm/min. To satisfy the standard, the deformation should be in the range of [20 mm, 40 mm] in the forefoot and [6 mm, 15 mm] in the heel under a vertical force of 400 N. The shaded zones in Figure 9(a) and (b) represent where the deformation

satisfied GB 14723-2008. All four configurations demonstrated acceptable stiffness in both dorsiflexion and plantarflexion. As shown in Figure 6, the cross-sectional area of configuration 3 in inversion and eversion was affected the most by forefoot bending. Thus, the minimum displacement occurred in configuration 3 when the platen displacement was 23.29 mm, which was the first to reach a reaction force of 400 N. This was followed by configuration 4, which had a displacement of 25.82 mm. Because the cross-sectional parameters of configuration 2 were derived from configuration 1 with identical shapes for inversion and eversion, configurations 1 and 2 had similar stiffness responses with displacements of 30.61 and 31.28 mm, respectively, in forefoot bending. In configurations 1 and 2, the curves were sharper when the displacement was less than 14.5 mm compared with after, which indicates that the inversion and eversion had not yet had a significant influence on the bending of the block. In heel bending, similar results were observed. Configuration 3 reached 400 N first followed by configurations 4, 2, and 1 with platen displacements of 6.04, 6.30, 6.76, and 7.08 mm, respectively.

In the inversion bending tests, configuration 3 exhibited the highest stiffness with a platen displacement of 3.93 mm at a reaction force of 400 N, followed by configurations 2 and 4 with identical displacements of 4.78 mm. This is because configurations 2 and 4 had the same cross-sectional parameters in inversion bending. Configuration 1 had the lowest stiffness with a platen displacement of 6.35 mm at 400 N. As shown in Figure 9, the curves of eversion bending were precisely according to the cross-sectional areas of the configurations with platen displacements of 3.61, 3.71, 5.05, and 6.36 mm for configurations 4, 3, 2, and 1, respectively.

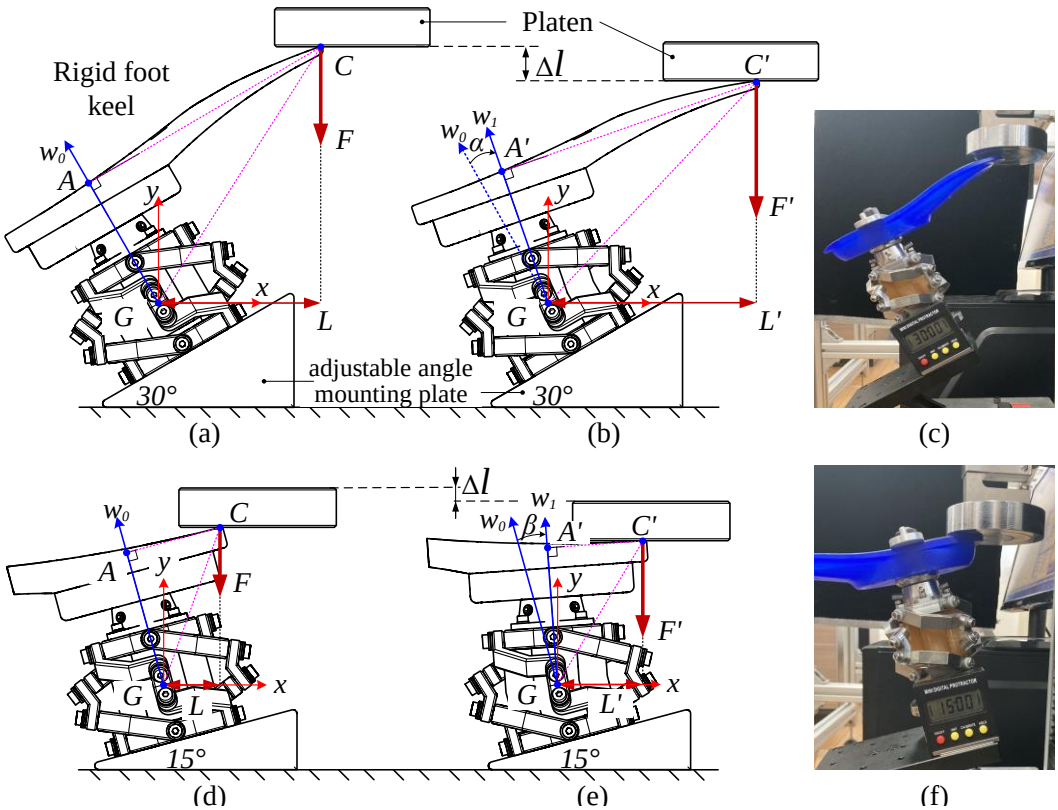

Figure 7 Schematic diagram for the mechanical testing of the 2-DOF CPA: (a, b) forefoot bending

and (d, e) heel bending. Initial setup: (c) forefoot bending and (f) heel bending.

The generated torque during bending in four directions was calculated as follows. As shown in Figure 7(a) and (b), the coordinate frame $\{G–x, y\}$ was established with the origin at the rotation center G, the x axis parallel to the ground, and the y-axis vertical to the x-axis. Point C is the contact point of the forefoot and platen attached to the load cell. The w_0 axis is along with the direction of the ankle joint, and line CA is normal to the w_0 axis. The parameters $|GA| = a$, $|AC| = b$. The coordinates of point C are denoted as $[P_{cx}, P_{cy}]^T$:

$$\begin{bmatrix} P_{Cx} \\ P_{Cy} \end{bmatrix} = \begin{bmatrix} \cos(\pi/6) & -\sin(\pi/6) \\ \sin(\pi/6) & \cos(\pi/6) \end{bmatrix} \begin{bmatrix} b \\ a \end{bmatrix} = \begin{bmatrix} \left(\sqrt{3}b - a\right)/2 \\ \left(\sqrt{3}a + b\right)/2 \end{bmatrix} \tag{13}$$

when the platen moves downward by Δl to change the force from F to F', the rigid foot keel is rotated about rotation center G of α, and points A and C are rotated to the new positions A' and C'. Hence, the coordinates of point C' can be obtained as follows:

$$\begin{bmatrix} P_{C'x} \\ P_{C'y} \end{bmatrix} = \begin{bmatrix} \cos(-\alpha) & -\sin(-\alpha) \\ \sin(-\alpha) & \cos(-\alpha) \end{bmatrix} \begin{bmatrix} \frac{\sqrt{3}b - a}{2} \\ \frac{\sqrt{3}a + b}{2} \end{bmatrix} = \begin{bmatrix} \frac{\sqrt{3}b - a}{2}\cos\alpha + \frac{\sqrt{3}a + b}{2}\sin\alpha \\ \frac{a - \sqrt{3}b}{2}\sin\alpha + \frac{\sqrt{3}a + b}{2}\cos\alpha \end{bmatrix} \tag{14}$$

Therefore, the platen displacement can be expressed as $\Delta l = P_{Cy} - P_{C'y} = \frac{\sqrt{3}a + b}{2} - \left(\frac{a - \sqrt{3}b}{2}\sin\alpha + \frac{\sqrt{3}a + b}{2}\cos\alpha \right)$. If $\kappa_1 = \frac{a - \sqrt{3}b}{2} < 0$ and $\kappa_2 = \frac{\sqrt{3}a + b}{2} > 0$, then Δl can be written as

$$\Delta l = \frac{\sqrt{3}a + b}{2} - \sqrt{\kappa_1^2 + \kappa_2^2}\sin\left(\alpha + (\pi + \sigma)\right) = \frac{\sqrt{3}a + b}{2} + \sqrt{a^2 + b^2}\sin(\alpha + \sigma) \tag{15}$$

where $\tan\sigma = \frac{\kappa_2}{\kappa_1} = \frac{\sqrt{3}a + b}{a - \sqrt{3}b} < 0$. Therefore, the relationship between the rotation angle α and displacement Δl from forefoot bending can be expressed as

$$\alpha = \arcsin\left(\frac{2\Delta l - \sqrt{3}a - b}{2\sqrt{a^2 + b^2}} \right) - \arctan\left(\frac{\sqrt{3}a + b}{a - \sqrt{3}b} \right) \tag{16}$$

Next, for the torque generated by forefoot bending, the moment arm $L_{forefoot}$ is easily written as

$$L_{forefoot} = P_{C'x} = \frac{\sqrt{3}a + b}{2}\sin\alpha + \frac{\sqrt{3}b - a}{2}\cos\alpha \tag{17}$$

According to equations (16) and (17), the torque generated by forefoot bending at a reaction force of 400 N is given by $T_{forefoot}=F\times L_{forefoot}$.

Similarly, the relationship between the rotation angle β and displacement Δl from heel bending can be expressed as

$$\beta = \arcsin\left(\frac{\Delta l - b\sin\left(\frac{\pi}{12}\right) - a\cos\left(\frac{\pi}{12}\right)}{\sqrt{a^2+b^2}}\right) - \arctan\left(\frac{b\sin\left(\frac{\pi}{12}\right) + a\cos\left(\frac{\pi}{12}\right)}{a\sin\left(\frac{\pi}{12}\right) - b\cos\left(\frac{\pi}{12}\right)}\right) \tag{18}$$

with the moment arm is

$$L_{heel} = \left(a\cos\left(\frac{\pi}{12}\right) + b\sin\left(\frac{\pi}{12}\right)\right)\sin\beta + \left(b\cos\left(\frac{\pi}{12}\right) - a\sin\left(\frac{\pi}{12}\right)\right)\cos\beta \tag{19}$$

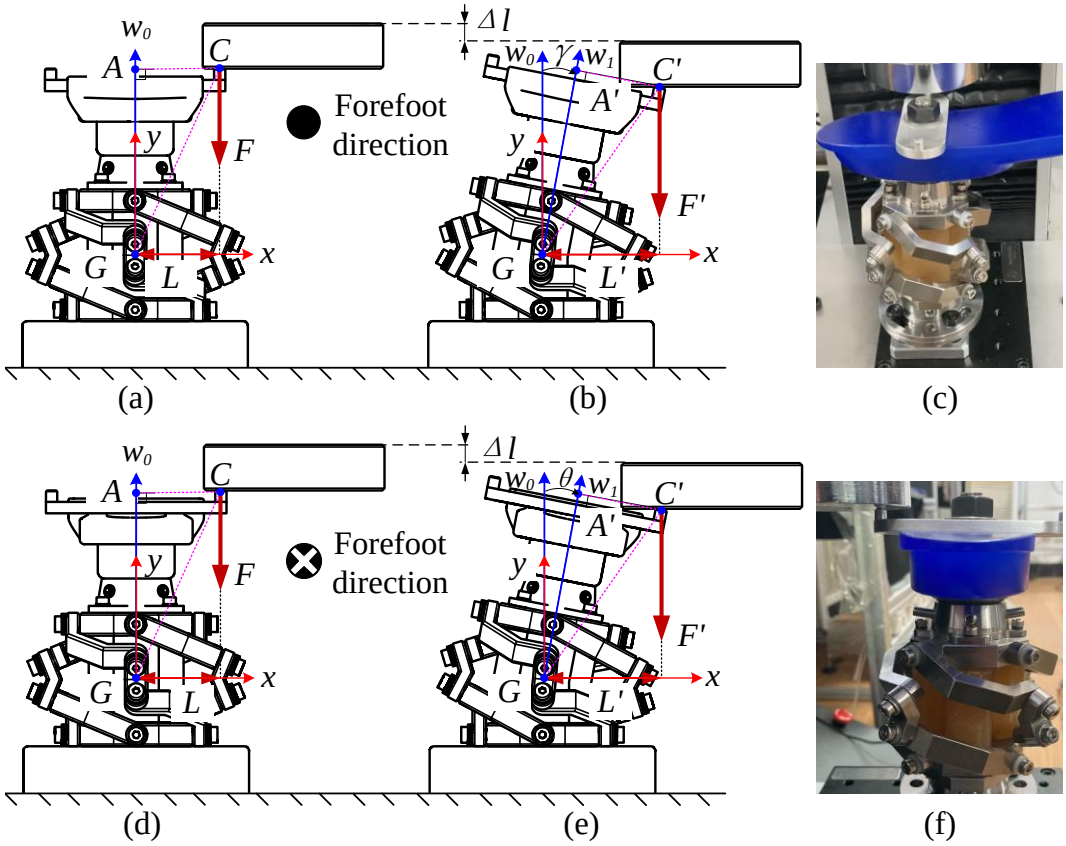

Figure 8 Schematic diagram of mechanical testing of the 2-DOF CPA during (a, b) inversion and (d, e) eversion. Initial setup: (c) inversion and (f) eversion.

Figure 8 shows that the rotation angle γ during inversion and rotation angle θ during eversion can be derived from the coordinates of points C and C' and displacement Δl:

$$\gamma \text{ or } \theta = \arcsin\left(\frac{\Delta l - a}{\sqrt{a^2 + b^2}}\right) - \arctan\left(-\frac{a}{b}\right) \tag{20}$$

The moment arms $L_{inversion}$ and $L_{eversion}$ are given by

$$\begin{cases} L_{inversion} = a\sin\gamma + b\cos\gamma \\ L_{eversion} = a\sin\theta + b\cos\theta \end{cases} \tag{21}$$

Table 1 presents the required parameters for calculated the torques generated by forefoot, heel, inversion, and eversion bending

Table 1 Parameters for mechanical testing using the uniaxial tensile test machine

Test conditions	|GA| = a	|AC| = b
Forefoot bending	72 mm	138 mm
Heel bending	69.4 mm	49 mm
Inversion and Eversion	82.4 mm	37.5 mm

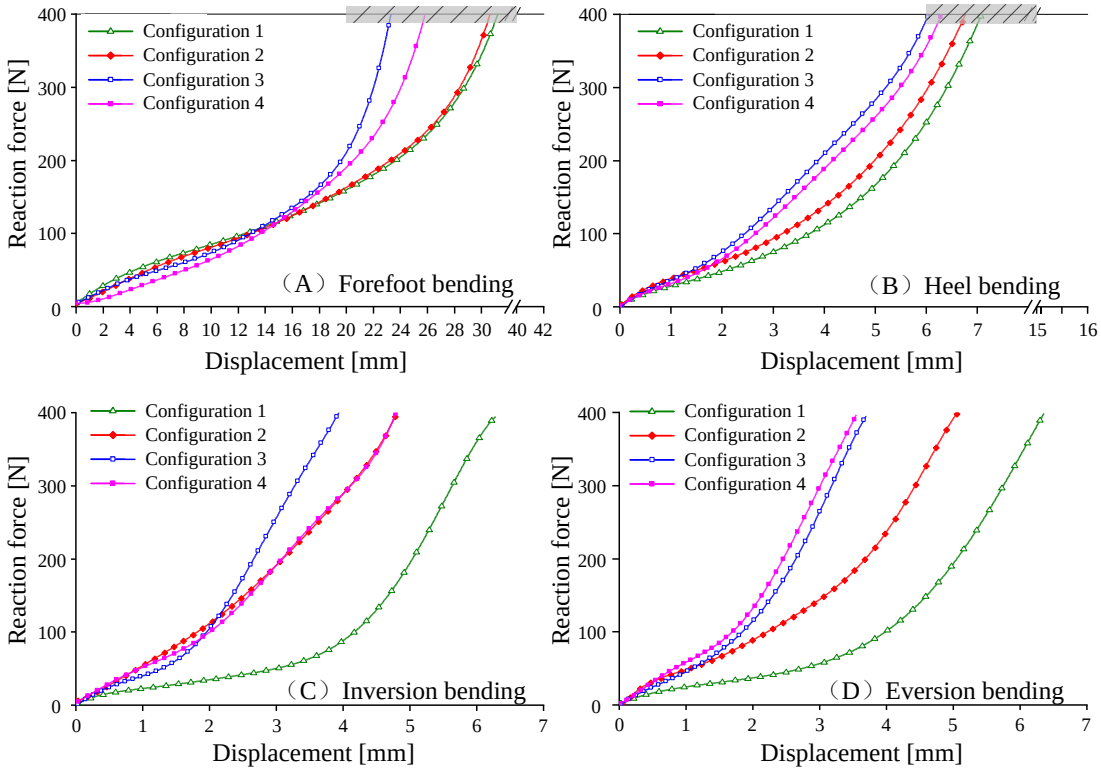

Figure 9 Performance of the 2-DOF CPA during (A) forefoot bending, (B) heel bending, (C) inversion bending, and (D) eversion bending.

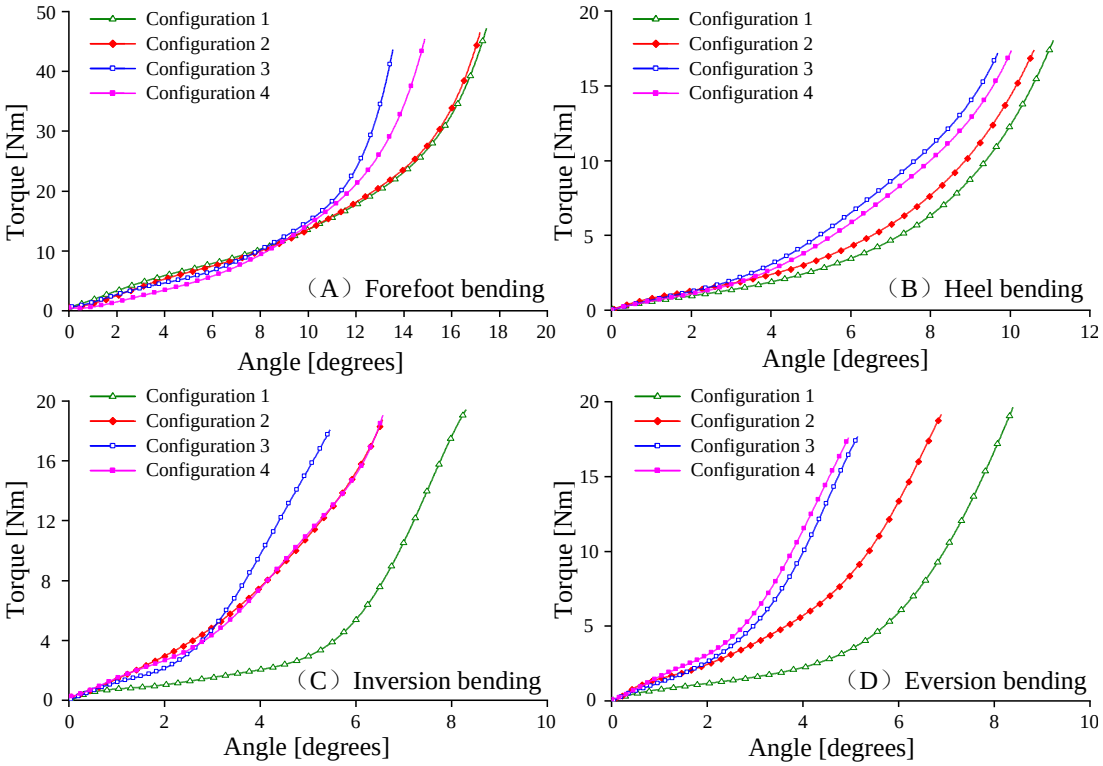

Figure 10 Generated torque with respect to the bending angle of the 2-DOF CPA during (A) forefoot bending, (B) heel bending, (C) inversion bending, and (D) eversion bending.

Figure 10 shows the generated torque of the 2-DOF CPAs in the four configurations with respect to the rotation angle at 400 N. During forefoot bending, the 2-DOF CPAs generate torques of [43.62 Nm, 46.52 Nm] with rotation angles of 13.54°, 14.88°, 17.17°, and 17.19° for configurations 3, 4, 2, and 1, respectively. Similarly, heel bending resulted in torques of [17.18 Nm, 18.02 Nm] with corresponding rotation angles of [9.69°, 11.07°]. During inversion bending, the maximum torque of 19.44 Nm was obtained by configuration 1 at an angle of 8.30°, and the minimum torque of 17.97 Nm was obtained by configuration 3 at an angle of 5.44°. For eversion bending, the maximum torque of 19.61 Nm was obtained by configuration 1 with an angle of 8.39°, and the minimum torque of 17.53 Nm was obtained by configuration 3 at an angle of 4.95°.

According to the section 6.2.4 in GB 14723-2008 standard, the angle range of inversion & eversion should beyond 5 degrees when a 50 Nm torque is applied on the corresponding directions. The measuring range of the uniaxial tensile test machine is 0-500 N. The inversion bending test results can be seen in Figure 10(C), under the force of 400 N, all the four configurations of 2-DOF CPAs with respect to the rotation angle reach 5 degrees and the applied moments are no more than 20 Nm. Assuming that the machine can continue applying force and generating moment of 50 Nm, the parallel mechanism will ultimately reach the limit range of motion due to the intrinsic geometric constraints of mechanism, as presented and indicated in Section 2.2. Hence, after reaching the limited position, the L-shaped link is in contact with the V-shaped link rigidly, and can sustain external torques of value that is greater than 500 N. Similarly,

eversion bending tests were conducted and the measurements showed feasible results.

The mechanical tests showed that the proposed 2-DOF CPAs retained sufficient elastic deformation and generated sufficient torque under the designated bending force of 400 N to satisfy GB 14723-2008 standard, which indicates that it can potentially guarantee gait comfort during dorsiflexion, plantarflexion, inversion, and eversion.

5 Clinical Validation

Next, a clinical validation was performed on the proposed 2-DOF CPAF, which consisted of two sessions. A below-knee dynamics analysis was performed with a specific subject wearing the 2-DOF CPAF for a complete gait cycle. Kinematic data were measured by using a Vicon™ optical motion capture system and Kistler™ force plate measurement system. We then assessed the metabolic effort required to walk on a treadmill with the proposed 2-DOF CPAF versus the subject's daily-use SACH. The energy expenditure was calculated by using a wearable metabolic system (COSMED™ K5), so the most efficient configuration could be determined. Table 2 lists the characteristics of the subject.

Table 2 Characteristics of subject

Gender	Age	Height	Weight	Amputation		
				Unilateral	Cause	Duration
Male	52	168 cm	87.5 kg	Left below-knee	Poliomyelitis + trauma	25 years

5.1 Dynamic Analysis

This study was approved by the Ethics Committee of the Second Hospital of Jilin University (Log#2021072) and performed according to the guidelines of the Declaration of Helsinki (2013) and the International Ethical Guidelines for Biomedical Research Involving Human Subjects (2002). The subject was recruited through a non-profit rehabilitation center for the disabled in Changchun City, China. Data were collected after the subjected consented to participate in the study.

5.1.1 Method:

The lower limb was represented as an articulated multi-segment system with six rigid segments (thighs, shanks, and feet). For the shank segment, the local coordinate system (LCS) was defined according to four palpable landmarks: the lateral and medial malleoli and the lateral and medial femoral epicondyles. The foot LCS was defined according to five markers: two on the lateral and medial malleoli, two on the first and fifth metatarsal heads, and one on the calcaneus. The origin of the shank LCS was at the midpoint of the lateral and medial epicondyles. The positions of the lateral and medial epicondyles and the midpoint of the lateral and medial malleoli were used to derive the LCS of the proximal biased shank. Similarly, the origin of the foot LCS was placed at the ankle joint center. The positions of the lateral and medial malleoli and the

first and fifth metatarsal heads were used to calculate the LCS of the foot [37]. The schematic diagrams of the location of the markers with its associated abbreviations for shank LCS and foot LCS calculation are shown in Figure 11.

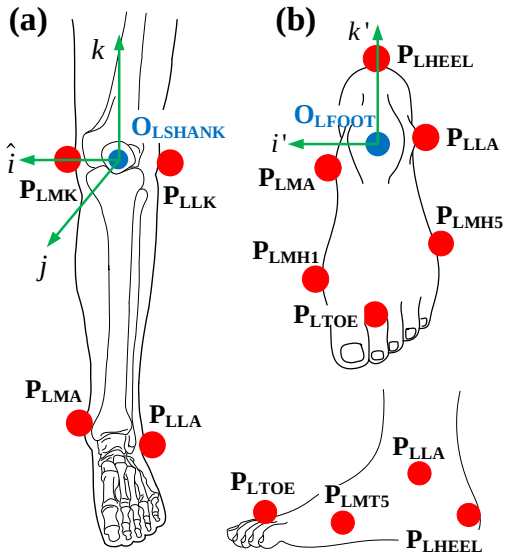

Abbreviations

- O_{LSHANK}: the origin of the left shank LCS
- O_{LFOOT}: the origin of the left foot LCS
- P_{LMK}: medial epicondyle of left leg
- P_{LLK} : lateral epicondyle of left leg
- P_{LMA}: medial malleoli of left leg
- P_{LLA} : lateral malleoli of left leg
- P_{LMH1}: the first metatarsal heads of left foot
- P_{LMH5}: the fifth metatarsal heads of left foot
- P_{LHEEL}: left heel
- P_{LTOE}: left toe

Figure 11 (a) The origin of the left shank LCS is located at the midpoint of the lateral and medial epicondyles (P_{LLK} and P_{LMK}). The positions of the lateral and medial epicondyles and the midpoint of the lateral and medial malleoli (P_{LLA} and P_{LMA}) can be used to derive the LCS of left shank. (b) The origin of the left foot LCS is at the ankle joint center. The positions of the lateral and medial malleoli (P_{LLA} and P_{LMA}) and the first and fifth metatarsal heads (P_{LMH1} and P_{LMH5}) can be used to calculate the LCS of the left foot.

For the shank segment, the LCS is defined from four palpable markers, the origin of the shank LCS is at the midpoint between the femoral epicondyles and can be calculated as:

$$\vec{O}_{LSHANK} = \frac{1}{2}\left(\vec{P}_{LLK} + \vec{P}_{LMK}\right) \tag{22}$$

To construct the shank LCS, we start by creating a superior unit vector based on an axis passing from the distal end (midpoint between the malleoli) to the segment origin as follows:

$$k = \frac{\vec{O}_{LSHANK} - \frac{1}{2}\left(\vec{P}_{LLA} + \vec{P}_{LMA}\right)}{\left|\vec{O}_{LSHANK} - \frac{1}{2}\left(\vec{P}_{LLA} + \vec{P}_{LMA}\right)\right|} \tag{23}$$

Next, a unit vector from the medial epicondyle to the lateral epicondyle is created as:

$$\hat{v} = \frac{\vec{P}_{LLK} - \vec{P}_{LMK}}{\left|\vec{P}_{LLK} - \vec{P}_{LMK}\right|} \tag{24}$$

Then we create the anterior unit vector from the cross product of the k and $\hat{v}$:

$$j = k \times \hat{v} \tag{25}$$

Last, the third lateral unit vector can be derived from the cross product:

$$\hat{i} = j \times k \tag{26}$$

Similarly, the origin of the left foot LCS is at the midpoint between the malleoli and can be given as:

$$\vec{O}_{LFOOT} = \frac{1}{2}\left(\vec{P}_{LLA} + \vec{P}_{LMA}\right) \tag{27}$$

The axially directed unit vector is created by subtracting the midpoint of the first and fifth metatarsal heads from the origin:

$$k' = \frac{\vec{O}_{LFOOT} - \frac{1}{2}\left(\vec{P}_{LMH1} + \vec{P}_{LMH5}\right)}{\left|\vec{O}_{LFOOT} - \frac{1}{2}\left(\vec{P}_{LMH1} + \vec{P}_{LMH5}\right)\right|} \tag{28}$$

Then the anterior unit vector and lateral unit vector can be expressed respectively as $j' = k' \times v'$ and $i' = j' \times k'$ with $v' = \frac{\vec{P}_{LLA} - \vec{P}_{LMA}}{\left|\vec{P}_{LLA} - \vec{P}_{LMA}\right|}$.

A segment model can be used to represent the foot as a free body in contact with a force–plate system. The dynamics of the *i*th segment are determined by Newton–Euler equations, where the ankle force (ground force) and net ankle moment [38, 39] of the able-bodied foot and ankle and the corresponding prosthesis can be represented as

$$\mathbf{F}_{gr} + \mathbf{F}_{gl} = \sum_{i=1}^{n}\left[m_i\left(\ddot{\mathbf{r}}_{ci} - \mathbf{g}\right)\right] \tag{29}$$

$$\mathbf{M}_{gr} + \mathbf{M}_{gl} = \sum_{i=1}^{n}\left[\mathbf{J}_{ci}\boldsymbol{\alpha}_i + \boldsymbol{\omega}_i \times \left(\mathbf{J}_{ci}\boldsymbol{\omega}_i\right)\right] - \sum_{i=1}^{n}\sum_{k=1}^{n_{ei}}\left(\mathbf{r}_{ek}^{(i)} \times \mathbf{F}_{ek}^{(i)}\right) - \sum_{i=1}^{n}\sum_{k=1}^{n_{ji}}\left(\mathbf{r}_{jk}^{(i)} \times \mathbf{F}_{jk}^{(i)}\right) \tag{30}$$

Details on the notation in equations (29) and (30) are listed in Appendix B. In a single stance, the ground force acting on the stance foot can be obtained directly from equation (29), and the smooth-transition assumption [38] is employed to solve the dynamics in the double support phase. In this study, the gait analysis for level-ground walking was conducted as follows:

Step 1: Define the shank and foot segment LCS.

Step 2: Estimate the pose data from motion capture system.

Step 3: Identify the anthropometry to the able-bodied side of the subject and the inertial characteristics of the prosthetic ankle-foot.

Step 4: Compute kinematics (e.g., angular velocities and accelerations) from the pose estimates.

Step 5: Combine the external forces acting on the lower-limb to the kinematics and finally compute the ankle forces and net moments.

The gait test for level-ground walking is conducted five times for each configuration at a normal speed, seeing in Figure 12.

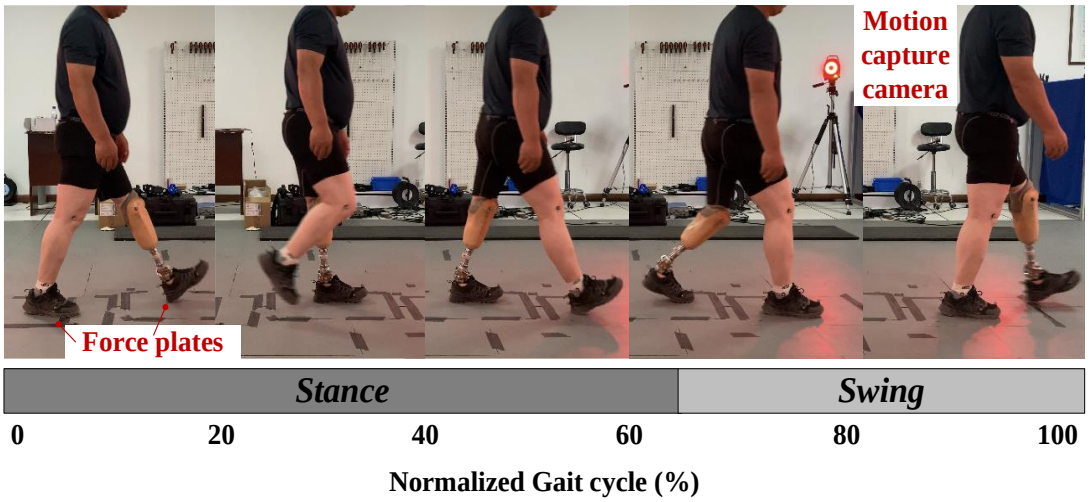

Figure 12 Level-ground walking test by an amputee wearing the proposed 2-DOF CPAF. The kinematics was measured by using a motion capture system and force–plate system.

5.1.2 Dynamic results of level-ground walking

Figure 13 to Figure 16 present the calculated force and torque in three dimensions during a single trial for the able-bodied foot and CPAF in the four configurations under level-ground conditions. They all followed normal patterns that broadly matched the published data [38]. The maximum moments generated on the ankle in three planes across several trials are presented in Figure 17 and Figure 18.

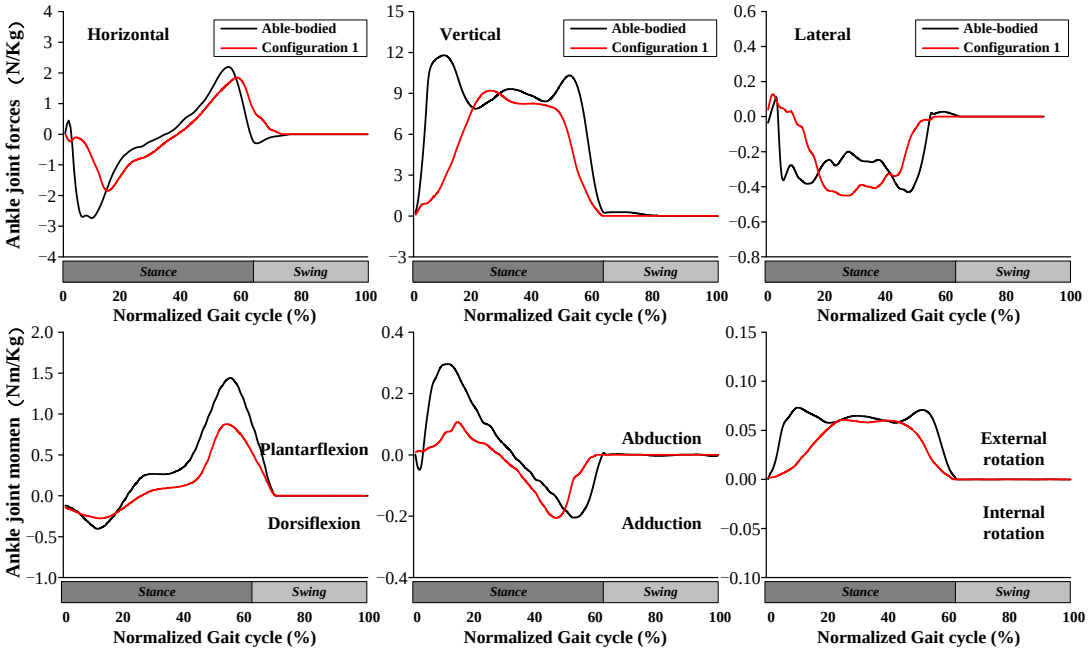

Figure 13 Resultant ankle joint forces and ankle moments normalized by the body mass of the subject for a single trial: configuration 1.

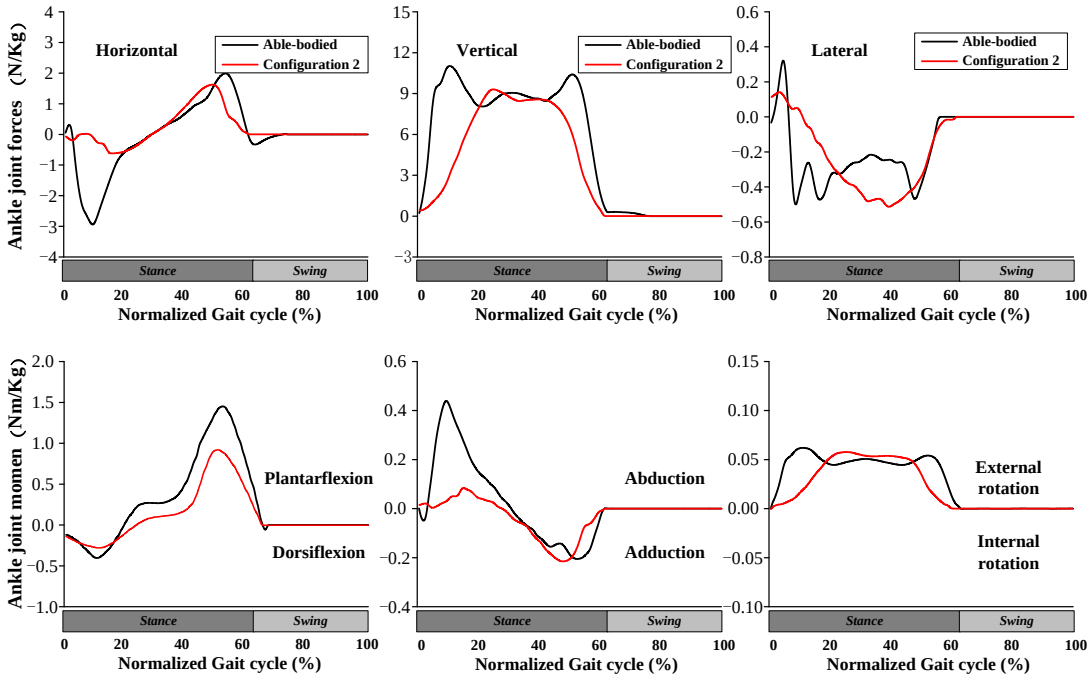

Figure 14 Resultant ankle joint forces and ankle moments normalized by the body mass of the subject for a single trial: configuration 2.

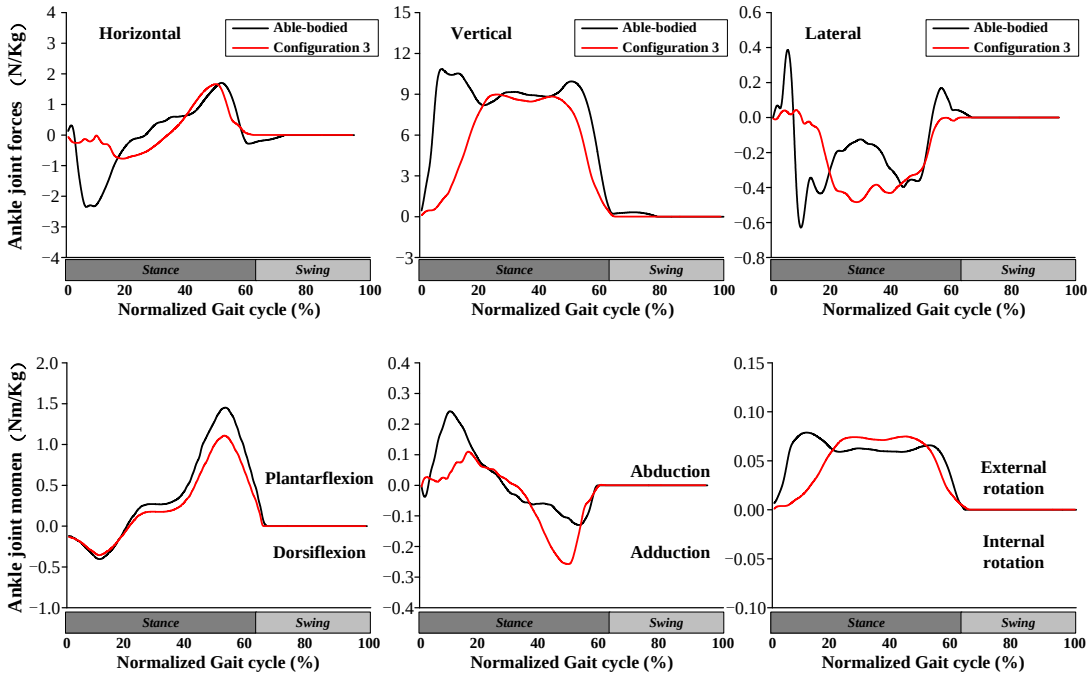

Figure 15 Resultant ankle joint forces and ankle moments normalized by the body mass of the subject for a single trial: configuration 3.

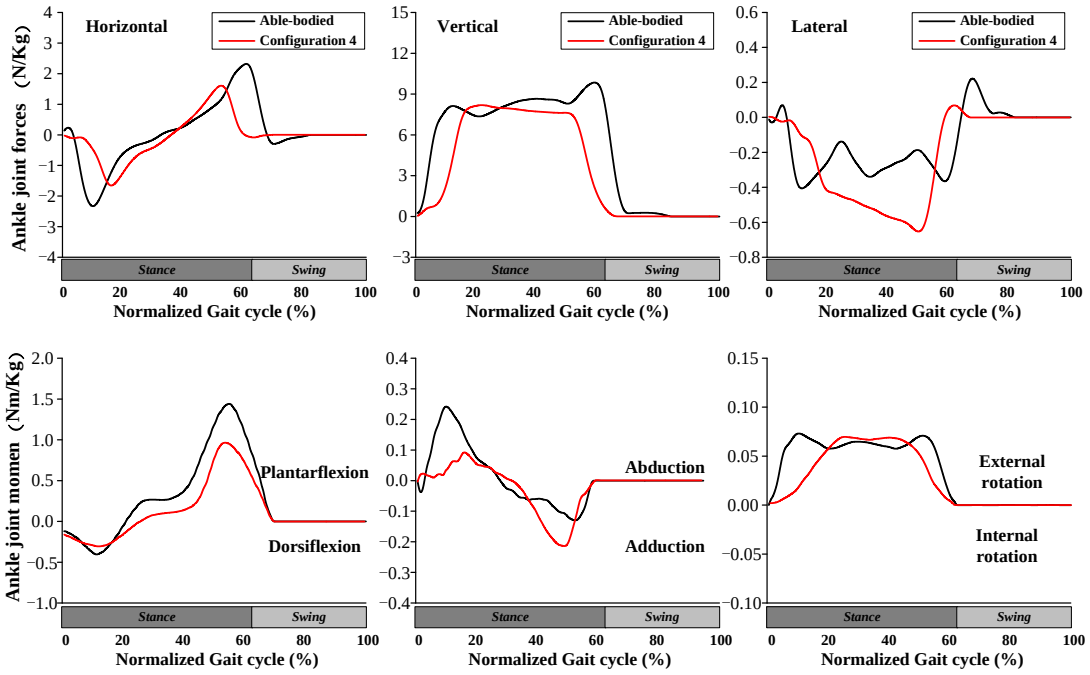

Figure 16 Resultant ankle joint forces and ankle moments normalized by the body mass of the subject for a single trial: configuration 4.

All four configurations followed nearly identical trends as the able-bodied ankle for the moments in dorsiflexion and plantarflexion. The peak moments were approximately the same in configurations 1 and 2 (T ≈ 0.014 Nm/kg) and in configurations 3 and 4 (T ≈ 0.053 Nm/kg). The different cross-sectional shapes of the support block meant that configurations 1 and 2 had significantly smaller peak moments than configurations 3 and 4. For plantarflexion, which mainly assists with push-off in the late stance phase, configuration 3 showed the best torque performance relative to the biological ankle with a difference of only 0.0344 Nm/kg.

As expected, no torque was generated during inversion in the frontal plane due to the balance requirement for level-ground walking, especially during the single stance phase. Regarding external rotation, the maximum moment was obtained by configuration 3. This implies that this configuration can contribute significantly to controlling eversion, which supports the results of the performance evaluation.

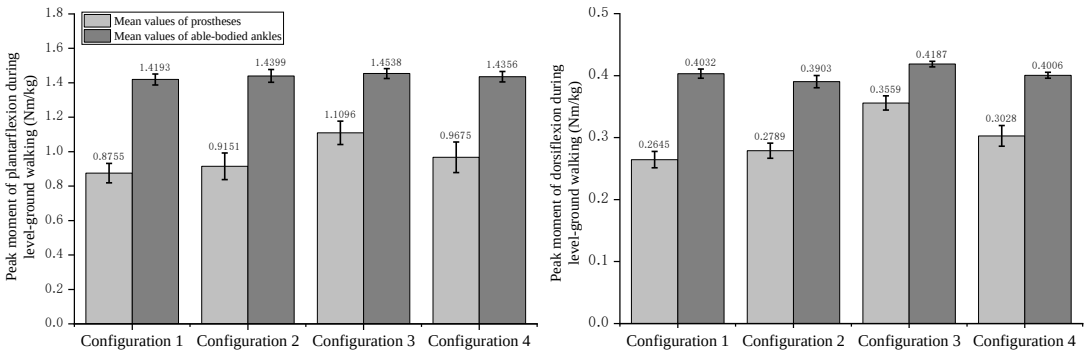

Figure 17 Peak ankle moments along the sagittal plane during the five trials. The light-gray columns represent the mean values for the CPAF, and the dark-gray areas show the mean values for the able-

bodied ankle.

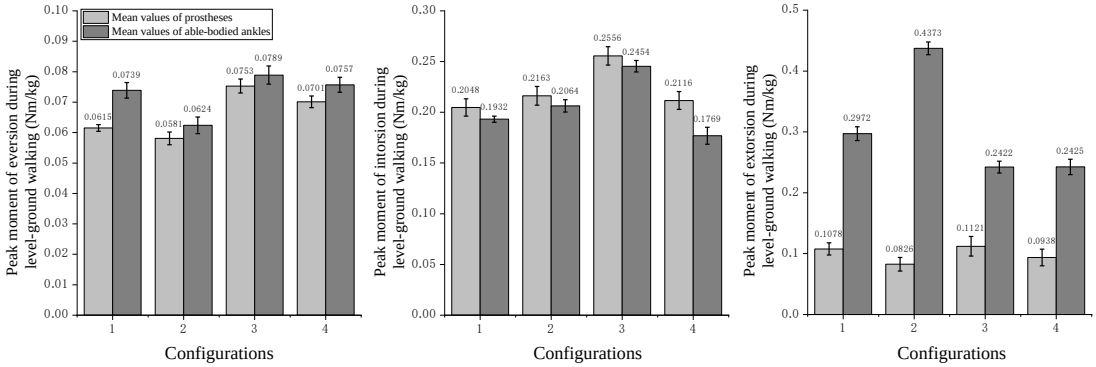

Figure 18 Peak ankle moments along the frontal and transverse planes during the five trials. The light-gray columns represent the mean values of the CPAF, and the dark-gray areas show the mean values of the able-bodied ankle in the four configurations. Note that no internal rotation occurred in the frontal plane, so no internal rotation graph is displayed.

5.2 Metabolic Test

A metabolic test was carried out for level-ground walking on a treadmill. The metabolic test was performed after the subject had become accustomed to wearing the 2-DOF CPAF in configurations 1–4. The test involved the subject walking on a level treadmill at a speed of 1.5 km/h for 5 min with each configuration. The subject was requested not to use any walking aids such as handrails while walking on the treadmill. The oxygen consumption data were recorded by using a metabolic system, as illustrated in Figure 19. The O_2 consumption was relatively stable with the 2-DOF CPAF configurations, although the fluctuations increased steadily over time.

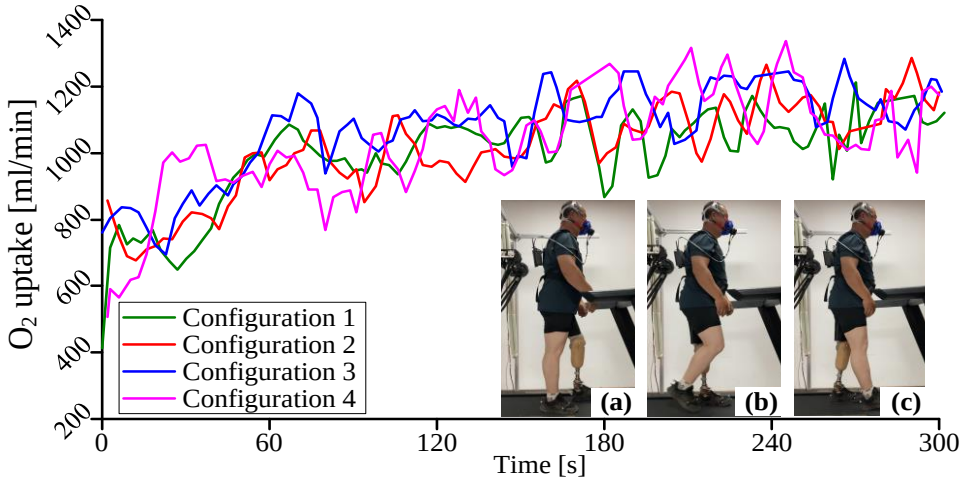

Figure 19 Measured O_2 uptake during level-ground walking on a treadmill at a speed of 1.5 km/h. The subject was wearing the 2-DOF CPAF and a metabolic apparatus (COSMED™ K5). (a)–(c) sagittal view.

The energy expenditure was determined from the oxygen uptake efficiency slope (OUES) [40, 41], which was calculated from the data measured during each test.

The OUES was firstly introduced as a useful index of cardiorespiratory functional reserve in 1996. The OUES reflects the regression curve relating the oxygen uptake

($\dot{V}O_2$: rate of oxygen consumption, ml/min) and rate of ventilation ($\dot{V}E$: rate of ventilation, L/min). The OUES is determined by equation

$$\dot{V}O_2 = a \log \dot{V}E + b \tag{31}$$

Taking the differential of the above equation by $\dot{V}E$ yields

$$\frac{d\dot{V}O_2}{d\dot{V}E} = a\left(\frac{1}{\ln 10\left(\dot{V}E\right)}\right) \tag{32}$$

where a = constant that represents the rate of increase in $\dot{V}O_2$ in response to $\dot{V}E$. Semilogarithmic transformation of the $\dot{V}E$ showed a linear relation between $\dot{V}O_2$ and log $\dot{V}E$ (Figure 20). OUES is the slope of the logarithmic regression curve expressing the relation between $\dot{V}O_2$ and $\dot{V}E$ represents the rate of increase $\dot{V}O_2$ in response to a given $\dot{V}E$. The OUES is a useful measure because it had been proved that it is highly correlated with $\dot{V}O_2$max and it can show the amount of energy expenditure without the subject having to endure maximum levels of exertion (OUES is not greatly affected by whether the exercise test was maximal or submaximal).

Thus, OUES is a variable that shows how effectively oxygen is extracted and taken into the body. The OUES plot indicates better energy efficiency as the slope of the line becomes steeper, demonstrating that the subject can maximize the use of oxygen with each breath.

We also carried out a metabolic test by using the SACH as a reference whose OUES was 1982.39. Figure 20 shows that the OUES of the subject wearing the 2-DOF CPAF, 2310.77 with configuration 1, 2323.86 with configuration 2, 2357.82 with configuration 3, and 2713.82 with configuration 4. Compared with the SACH, this represents improvements of 16.56%, 17.23%, 18.94%, and 36.90% in oxygen use with configurations 1, 2, 3, and 4, respectively. The steep OUES indicates that the subject was most efficient when wearing the 2-DOF CPAF in configuration 4 and that the subject was using oxygen aerobically rather than anaerobically.

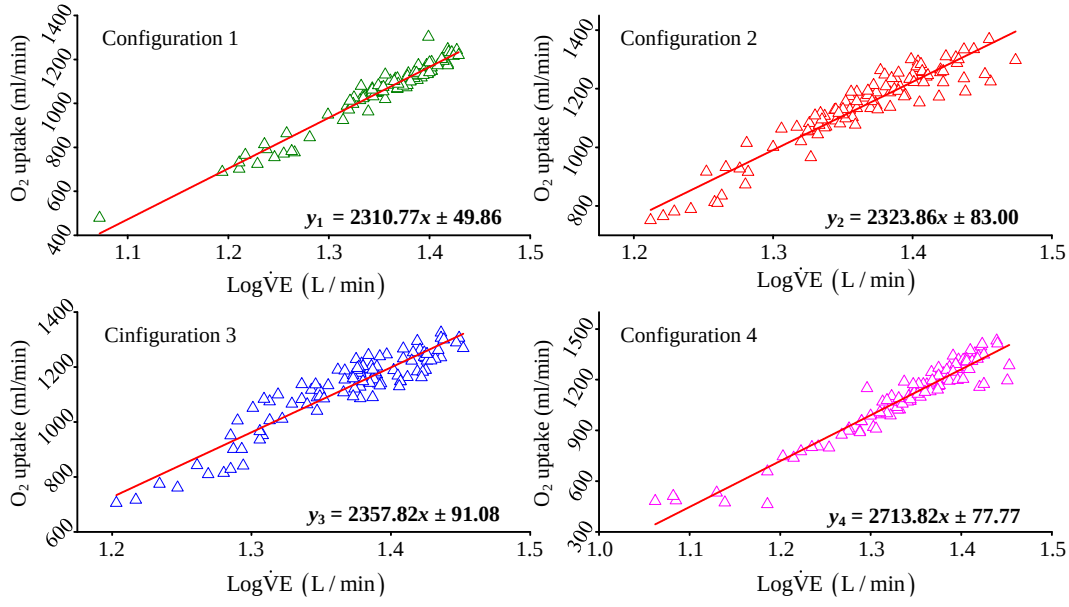

Figure 20 Differences in the oxygen uptake efficiency slope (OUES) for four configurations.

6 Conclusion

In this paper, we describe the parallel kinematic mechanism used to develop a 2-DOF CPAF and the specific requirements that had to be satisfied. The 2-DOF PM is a novel pointing mechanism that executes equal-diameter spherical motion, and it can be used to assist patients with achieving a natural gait motion with the help of a compliant component. Performance bench tests were carried out on a prototype with different configurations of the support block. The results showed that the proposed 2-DOF CPAF is lightweight and compact with an appropriate range of motion and mechanical torque. A unilateral transtibial amputee was asked to perform tasks to evaluate the proposed prosthesis for level-ground walking. First, a dynamic analysis was performed on a complete gait cycle. The results showed that the 2-DOF CPAF provides good gait movement and sufficient ankle torque for level-ground walking. Second, we carried out a metabolic test to estimate the energy consumption. The OUES results indicated that configuration 4 was the most efficient and allowed the subject to use oxygen aerobically rather than anaerobically.

Future work will involve a more thorough biomechanical characterization of the effects of the compliant component during different mobility tasks such as ascending stairs and walking on uneven terrain. More subjects should be considered for the clinical validation because the velocity, body mass, and leg length are all known to influence the metabolic energy consumption during gait analysis significantly.

Declaration of Competing Interest

This is to confirm that the authors of this paper declare no conflict of interest.

Acknowledgements

This work is partly supported by the National Key R&D Program of China under Grant No.2018YFC2001301.

Appendix A

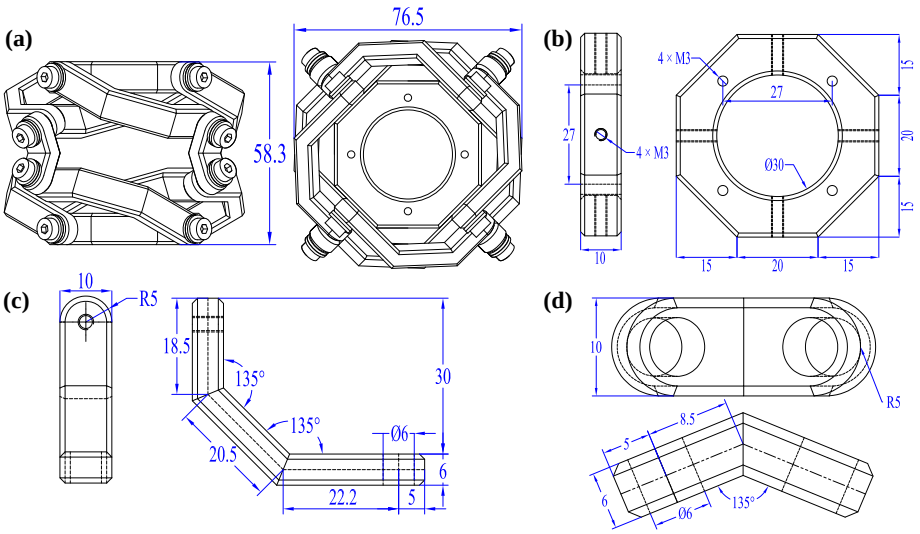

Figure 21 The geometric parameters of the parallel mechanism (Omni-Wrist III) used in the CPAF

prototype (unit, mm). (a) the overall structure (b) the moving platform & fixed base (c) the L-shaped link and (d) the V-shaped link.

Table 3 The structural parameters of the parallel mechanism (Omni-Wrist III) used in the CPAF prototype

Component	Mass	Material
Moving platform & base	102.24 g	AISI 304 Stainless steel
L-shaped link	28 g	
V-shaped link	9 g	
Total with screws, spacers, etc.	520.28 g	

Appendix B

The notions of equations (29) and (30): $\mathbf{F}_{gr}$/ $\mathbf{M}_{gr}$ and $\mathbf{F}_{gl}$/$\mathbf{M}_{gl}$ represent the ground forces/net moments on right foot and left foot respectively, m_i is the mass of ith segment, $\ddot{\mathbf{r}}_{ci}$ denotes the translational acceleration vector of the ith segment's mass center, $\mathbf{J}_{ci}$ represents the inertia tensor around the mass center of the ith segment, $\boldsymbol{\alpha}_i$ and $\boldsymbol{\omega}_i$ mean the angular acceleration vector and velocity vector of the ith segment respectively, $\mathbf{F}_{jk}^{(i)}$ means the kth joint force vector acting on the ith segment and $\mathbf{r}_{jk}^{(i)}$ means the position vector of the kth joint force from the mass center of the ith segment, $\mathbf{F}_{ek}^{(i)}$ means the kth external force vector acting on the ith segment and $\mathbf{r}_{ek}^{(i)}$ means the position vector of the kth external force from the mass center of the ith segment, $\mathbf{g}$ is the gravitational vector.

References

[1] D.J. Sanderson, P.E. Martin, Lower extremity kinematic and kinetic adaptations in unilateral below-knee amputees during walking, Gait & Posture, 6 (1997) 126-136.

[2] A.K. Silverman, N.P. Fey, A. Portillo, J.G. Walden, G. Bosker, R.R. Neptune, Compensatory mechanisms in below-knee amputee gait in response to increasing steady-state walking speeds, Gait & Posture, 28 (2008) 602-609.

[3] B.J. Hafner, J.E. Sanders, J. Czerniecki, J. Fergason, Energy storage and return prostheses: does patient perception correlate with biomechanical analysis?, Clinical Biomechanics, 17 (2002) 325-344.

[4] T. Lenzi, M. Cempini, L.J. Hargrove, T.A. Kuiken, Design, development, and validation of a lightweight nonbackdrivable robotic ankle prosthesis, IEEE/ASME Transactions on Mechatronics, 24 (2019) 471-482.

[5] M. Schlafly, K.B. Reed, Novel passive ankle-foot prosthesis mimics able-bodied ankle angles and ground reaction forces, Clinical Biomechanics, 72 (2020) 202-210.

[6] A.B. During, S. Sivarasu, G. Vicatos, An attempt to improve stance mechanics of trans-tibial amputee gait by the design of a modular ankle joint prosthetic, Proceedings of the 2018 Design of Medical Devices Conference, Minneapolis, Minnesota, USA. April 9–12, 2018. V001T03A017.

[7] C.L. Brockett, G.J. Chapman, Biomechanics of the ankle, Orthopaedics and Trauma, 30 (2016) 232-238.

[8] G.N. Askew, L.A. McFarlane, A.E. Minetti, J.G. Buckley, Energy cost of ambulation in trans-tibial amputees using a dynamic-response foot with hydraulic versus rigid 'ankle': insights from body centre of mass dynamics, Journal of NeuroEngineering and Rehabilitation, 16 (2019) 39.
[9] S. Debta, K. Kumar, Biomedical design of powered ankle- foot prosthesis – A Review, Materials Today: Proceedings, 5 (2018) 3273-3282.
[10] A.H. Hansen, D.S. Childress, S.C. Miff, S.A. Gard, K.P. Mesplay, The human ankle during walking: implications for design of biomimetic ankle prostheses, Journal of Biomechanics, 37 (2004) 1467-1474.
[11] T. Pain, S. Belmana, F. Claeyssen, E. Prevost, A. Weickman, F. Bourgain, O. Sosnicki, Beam steering mechanism for earthcare atmospheric lidar instrument ATLID: an ultra-stable piezoelectric tip tilt mechanism, International Conference on Space Optics (ICSO2016), Biarritz, France, 2017, pp. 31.
[12] E. G.Merriam, J. Jones, S. Magleby, L. Howell, Monolithic 2 DOF fully compliant space pointing mechanism, Mechanical Sciences, 4 (2013) 381-390.
[13] J. Zhang, Y. Song, D. Liang, Mathematical modeling and dynamic characteristic analysis of a novel parallel tracking mechanism for inter-satellite link antenna, Applied Mathematical Modelling, 93 (2021) 618-643.
[14] Y. Song, Y. Qi, G. Dong, T. Sun, Type synthesis of 2-DoF rotational parallel mechanisms actuating the inter-satellite link antenna, Chinese Journal of Aeronautics, 29 (2016) 1795-1805.
[15] S. Iqbal, A.I. Bhatti, M. Akhtar, S. Ullah, Design and robustness evaluation of an H∞ loop shaping controller for a 2DOF stabilized platform, 2007 European Control Conference (ECC), 2007, pp. 2098-2104.
[16] H. Jeong, S. Baek, W. Kim, B.J. Yi, Development of a spherical 2-dof wrist employing spatial parallelogram structure, 2020 IEEE/RSJ International Conference on Intelligent Robots and Systems (IROS), 2020, pp. 6434-6439.
[17] Y. Hiroya, I. Hiroaki, H. Shigeo, Design of large motion range and heavy duty 2-dof spherical parallel wrist mechanism, 25 (2013) 294-305.
[18] H. Huang, E. Dong, M. Xu, J. Yang, K.H. Low, Mechanism design and kinematic analysis of a robotic manipulator driven by joints with two degrees of freedom (DOF), Industrial Robot: An International Journal, 45 (2018) 34-43.
[19] J. Mei, J. Zang, Y. Ding, S. Xie, X. Zhang, Rapid and automatic zero-offset calibration of a 2-dof parallel robot based on a new measuring mechanism, Strojniski Vestnik, Journal of Mechanical Engineering, 63 (2017) 715-724.
[20] G. Palmieri, On the positioning error of a 2-DOF spherical parallel wrist with flexible links and joint-an FEM approach, Mech. Sci., 6 (2015) 9-14.
[21] D. Corinaldi, M. Callegari, J. Angeles, Singularity-free path-planning of dexterous pointing tasks for a class of spherical parallel mechanisms, Mechanism and Machine Theory, 128 (2018) 47-57.
[22] J. Yu, K. Wu, G. Zong, X. Kong, A comparative study on motion characteristics of three two-degree-of-freedom pointing mechanisms, Journal of Mechanisms and Robotics, 8(2) (2016) 028027.
[23] J.V. Harrison, J.L. Gallagher, E.J. Grace, An algorithm providing all-attitude

capability for three-gimballed inertial systems, IEEE Transactions on Aerospace and Electronic Systems, AES-7 (1971) 532-543.
[24] S. Yu, J. Zhang, W. Li, X. Yang, New decoupled 2-dof parallel mechanism with fully spherical workspace, Journal of Physics: Conference Series, IOP Publishing, 2020, pp. 012104.
[25] J. Sun, L. Shao, L. Fu, X. Han, S. Li, Kinematic analysis and optimal design of a novel parallel pointing mechanism, Aerospace Science and Technology, 104 (2020) 105931.
[26] M. Rosheim, G. Sauter, New high-angulation omni-directional sensor mount, International Symposium on Optical Science & Technology, Seattle WA(US), 2002, pp. 163-174.
[27] J. Sofka, V. Skormin, V. Nikulin, D.J. Nicholson, Omni-wrist iii - a new generation of pointing devices. part i. laser beam steering devices - mathematical modeling, IEEE Transactions on Aerospace and Electronic Systems, 42 (2006) 718-725.
[28] K. Wu, J. Yu, G. Zong, X. Kong, A family of rotational parallel manipulators with equal-diameter spherical pure rotation, Journal of Mechanisms and Robotics, 6 (2013).
[29] J. Sofka, V. Skormin, V. Nikulin, D.J. Nicholson, Omni-Wrist III - a new generation of pointing devices. Part II. Gimbals systems - control, IEEE Transactions on Aerospace and Electronic Systems, 42 (2006) 726-734.
[30] J. Yu, X. Dong, X. Pei, X. Kong, Mobility and singularity analysis of a class of two degrees of freedom rotational parallel mechanisms using a visual graphic approach, Journal of Mechanisms and Robotics, 4(4) (2012) 041006.
[31] Z. Duan, J. Yu, X. Kong, Axode characteristic of 4-4r parallel pointing mechanism, ASME 2015 International Design Engineering Technical Conferences and Computers and Information in Engineering Conference, Boston, Massachusetts, USA, 2015.
[32] X. Kong, J. Yu, D. Li, Reconfiguration analysis of a two degrees-of-freedom 3-4r parallel manipulator with planar base and platform, Journal of Mechanisms and Robotics, 8(1) (2016) 011019.
[33] K. Wu, J. Yu, G. Zong, X. Kong, Type synthesis of 2-dof rotational parallel manipulators with an equal-diameter spherical pure rolling motion, ASME 2013 International Design Engineering Technical Conferences and Computers and Information in Engineering Conference, Portland, Oregon, USA, 2013.
[34] J. Yu, J. Yu, K. Wu, X. Kong, Design of constant-velocity transmission devices using parallel kinematics principle, ASME 2014 International Design Engineering Technical Conferences and Computers and Information in Engineering Conference, Buffalo, New York, USA, 2014.
[35] J.J. Cervantes-Sánchez, J.C. Hernández-Rodríguez, E.J. González-Galván, On the 5r spherical, symmetric manipulator: workspace and singularity characterization, Mechanism and Machine Theory, 39 (2004) 409-429.
[36] S.A.o.T.P.s.R.o. China, Modular units of the lower limb prosthesis, GB 14723-2008 (2008).
[37] D. Robertson, G. Caldwell, J. Hamill, G. Kamen, S. Whittlesey, Research methods in biomechanics - 2nd edition, 2014.
[38] L. Ren, R.K. Jones, D. Howard, Whole body inverse dynamics over a complete

gait cycle based only on measured kinematics, Journal of Biomechanics, 41 (2008) 2750-2759.
[39] D.A. Winter, Biomechanics and motor control of human movement - 4th edition, 2009.
[40] C.A. Miller, D.M. Hayes, B.E. Brooks, K.Y. Sloan, P.G. Sloan, The effect of body weight support on energy expenditure in an individual with high-level lower extremity amputation, Physical therapy, 99 (2019) 258-265.
[41] R. Baba, M. Nagashima, M. Goto, Y. Nagano, M. Yokota, N. Tauchi, K. Nishibata, Oxygen uptake efficiency slope: a new index of cardiorespiratory functional reserve derived from the relation between oxygen uptake and minute ventilation during incremental exercise, Journal of the American College of Cardiology, 28(6) (1996):1567-72.